

# Electron spin decoherence in geometrically ordered nuclear spin baths

Jiangyang You,\* Dejana Carić, Boris Rakvin, Zoran Štefanić, Krunoslav Užarević, and Marina Kveder

*Rudjer Bošković Institute, Division of Physical Chemistry, Bijenička 54 10000 Zagreb, Croatia*

E-mail: Jiangyang.You@irb.hr

## Abstract

A global theoretical survey of electron spin decoherence decay at all single crystal orientations is performed for paramagnetic centres in  $\beta$ -malonic acid (MA) using nuclear spin bath model and cluster correlation expansion (CCE) method. The outcome is subsequently confirmed by experiment. The combined result verifies the simple principle that the extrema of the decoherence decay time scales are determined by the orientation of the nearest nuclear spin pairs in the bath, which links the decoherence decay directly to the matrix material structure and thus making it a potential *in-situ* structure indicator in EPR experiments. Also deduced from the same principle is that amorphorization reduces the decay time scale, which is verified both by theoretical calculation and experimental measurements on the new amorphous malonic acid polymorph prepared by mechanical milling.

# Introduction

The electron spin phase memory/decoherence decays in Hahn spin echo and its multiple pulse generalizations, the Carr-Purcell-Meiboom-Gill (CPMG) (and, recently, the Uhrig) dynamical decoupling pulse sequences,<sup>1</sup> are essential part of the pulsed electron paramagnetic resonance (EPR) measurements.<sup>2</sup> On the other hand, the understanding of the decoherence decay itself (decay time  $T_m$  and decay profile function(s)) has only taken a quantum leap forward in the last decade, when the quantum many body nuclear spin bath model<sup>3</sup> was developed for studying the decoherence profile of solid state quantum computer memory units (qubits).<sup>4</sup> In this model an isolated central electron spin's coherence is reduced by the hyperfine coupling to many ( $10^2 - 10^4$ ) surrounding nuclear spins, which are interacting with each other via dipolar couplings. The quantum many body dynamics of the nuclear spin bath model can be solved in two dedicative methods, the linked cluster expansion (LCE),<sup>5</sup> which is essentially a perturbative expansion over the nuclear dipolar coupling and particularly suitable for semiconductor qubits, and the cluster correlation expansion (CCE)<sup>6</sup> which employs a nonperturbative nuclear spin cluster based expansion and thus significantly extends the applicability of the nuclear spin bath model.<sup>4,7-9</sup> Combined with appropriate solving methods, the nuclear spin bath model has been proven to be highly successful in predicting the decoherence behavior of various systems directly from their structure inputs.<sup>4,7,8,10</sup> An extension to the electron-electron spin interaction has also been studied.<sup>9</sup> It becomes then natural to consider the inverse problem: How to use the nuclear spin bath model framework to connect  $T_m$  back to the structure of the matrix material and, if possible, turn the experimentally long known orientational variation of  $T_m$  into a quantitative indicator for crystal structure and/or structure changes. This furnishes the main aim of this article.

In literature it has been pointed out theoretically that in phosphorous-silicon (P:Si) qubits<sup>10</sup>  $T_m$  can extend significantly (> 2 times) when magnetic field is aligned to the crystal direction [111], where the dipolar interaction between (all) nearest <sup>29</sup>Si nuclear spin pairs vanishes. Magnetic field orientation dependence was also used to resolve single <sup>13</sup>C

pairs in nitrogen-vacancy (NV)-diamond system.<sup>11</sup> Two corollaries can be made from these observations: First, the maximum(s) of  $T_m$  among magnetic field orientations reflect the crystal structure of the matrix material through the minimal allowable distance between nuclear spins in the bath. Second, if a structure modification can change the orientations and/or distances of the nearest nuclear spin pairs in the bath, it would influence central electron spin  $T_m$  as well. In this work we realize both aspects in an EPR benchmark material  $\beta$ -malonic acid (MA), ideal for our study because lattice symmetry sets each of the first three nearest proton pair classes to be parallel to each other. The first corollary is observed in a single crystal rotation experiment and the second is achieved via mechanical milling amorphorization of polycrystalline MA.

## Results and discussion

Prior work on single crystal MA at a single orientation<sup>7</sup> has shown that the nuclear spin bath provides the main contribution to the electron spin decoherence decay in Hahn echo pulse sequence. We therefore first survey theoretically decoherence decays at various single crystal orientations using the nuclear spin bath model and CCE method. We choose to use the following spin bath Hamiltonian:

$$H_{\text{bath}} = H_{\text{Zeeman}} + H_{\text{eN}} + H_{\text{NN}}, \quad (1)$$

$$H_{\text{Zeeman}} = \mu_B g_{zz} B_0 S^z - \gamma_p \sum_i B_0 I_i^z, \quad (2)$$

$$H_{\text{eN}} = \sum_i E_i S^z I_i^z, \quad (3)$$

$$H_{\text{NN}} = \sum_{i < j} D_{ij} (I_i^+ I_j^- + I_i^- I_j^+ - 4 I_i^z I_j^z), \quad (4)$$

in which all symbols bear their usual meanings.<sup>3</sup> Both the electron-nuclear spin hyperfine coupling  $E_i$  and nuclear spin-nuclear spin couplings  $D_{ij}$  are considered to be of the point-

dipolar type, i.e.

$$E_i = \gamma_e \gamma_p \frac{3z_i^2 - |\vec{r}_i|^2}{|\vec{r}_i|^5}, \quad (5)$$

$$D_{ij} = \gamma_p^2 \frac{3(z_i - z_j)^2 - |\vec{r}_i - \vec{r}_j|^2}{4|\vec{r}_i - \vec{r}_j|^5}, \quad (6)$$

where  $\vec{r}_i$  is the the coordinate of  $i$ -th proton in the bath.

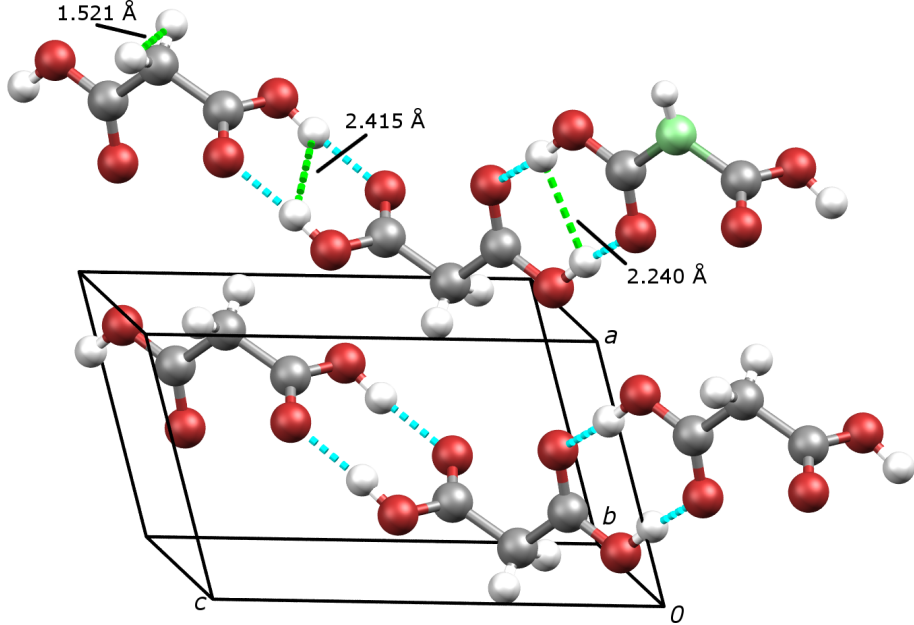


Figure 1: Crystal structure of  $\beta$ -malonic acid (triclinic, space group  $P\bar{1}$ , CSD:MALNAC02<sup>12</sup>) with MA radical (upper right corner) embedded in: We assume the electron density is confined on the radical carbon atom (light green) and neglect all structure differences between the radical and pristine molecule other than the  $\alpha$ -proton position. Hydrogen bonds between molecules (light blue), first three closest proton pairs (green), and distances between protons in each of these three type of pairs (in  $\text{\AA}$ ) are also given here.

We consider the nuclear spin bath consisting of one MA radical<sup>13</sup> and 149 MA molecules, 599 protons in total. CCE till 4-clusters is caculated. A Fibonacci grid<sup>14</sup> with 251 points is used to sample the orientations. A heat map (Fig. 2) is generated by combining the Fibonacci grid and its inversion image as the grid is not inversion invariant.

Globally, Fig. 2 exhibits features very similar to those reported in literature:<sup>10</sup>  $T_m$  changes about three times from minimum to maximum in our case. The maximums of  $T_m$  occur in

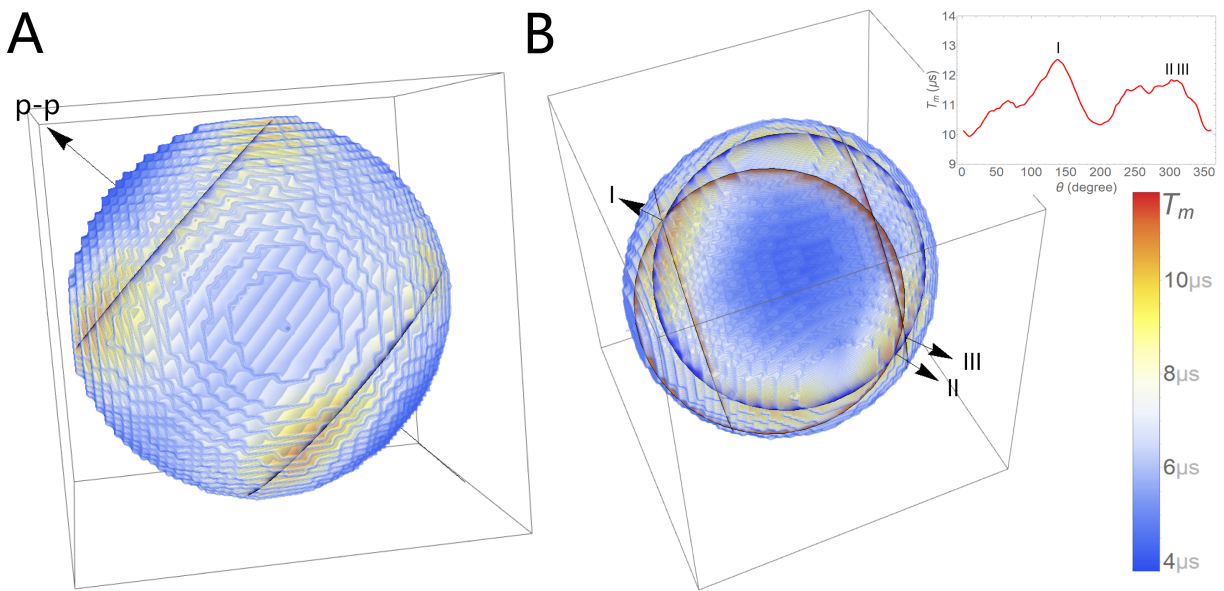


Figure 2: Orientational distribution of  $T_m$  from nuclear spin bath model calculation. **A:** Global distribution, two magic angle rings (blue) can be seen passing right through the highlighted  $T_m$  maximum. The nearest proton pair direction is labelled by the “p-p” arrow. **B:** Details of the maximum/magic angle ring: I, II and III mark the positions of the calculated maximums on the ring, as shown in the insert. They correspond very well with the positions where the magic angle ring of the closest neighbours (blue) intersects with the magic angle rings of the second and third closest neighbours (orange).

the vicinity of two rings, on which the dipolar coupling (6) of all nearest pairs vanish. (Such orientations are set by the condition of being  $\arccos \frac{1}{\sqrt{3}} \simeq 54.7^\circ$  to the nearest proton pair direction, long known as “magic angle” in magnetic resonances.) It is further observed that the fluctuation of  $T_m$  around the magic angle ring is determined by the intersection with the magic angle rings of second and third closest pairs: A nearly triple intersection spot corresponds to the highest  $T_m$  value, while the other two slightly more split ones to the pair of second highest values, as shown in Fig. 2B.

Two experiments are set up to test the theory prediction:

The first experiment aims at the *relative* distribution of  $T_m$ , i.e. directions of  $T_m$  maximums and minimums. In this experiment the crystal orientation dependence of  $T_m$  is measured on a  $\gamma$ -irradiated single crystal MA at 80 K with crystal rotating around three orthogonal axes: 1)  $a' = c^* \times b$ , 2)  $c^* = a \times b$  and 3)  $b$ . At each orientation EPR spectrum detected via magnetic field sweep and Hahn echo signal time decay are collected.  $T_m$ ’s are calculated by fitting the recorded data as monoexponential decay.

Theoretical values of  $T_m$  are obtained in two steps: First, total decoherence decay profiles  $f_{total}(t)$  are generated for various sampling orientations as products of the nuclear spin bath model profiles  $f_{bath}(t)$  and an isotropic monoexponential decay  $f_{mono}(t) = e^{-\frac{t}{\tau}}$  put by-hand:

$$f_{total}(t) = f_{bath}(t) \times f_{mono}(t). \quad (7)$$

$\tau = 7.5 \mu s$  is chosen to scale the theoretical  $T_m$  to the experiment. Isotropy ensures that peak positions remain the same. Finally,  $f_{total}(t)$ ’s are fitted monoexponentially to obtain theoretical  $T_m$ ’s. The span of the theoretical and experimental values of  $T_m$  between rotation planes a found to match very well: A large variation of  $T_m$  occurs in the rotation plane 1 because it closely passes by the nearest pair orientation, while rotation planes 2 and 3 share a similarly small variety of  $T_m$  values.

Theoretical and experimental results are further compared via the following independent

orientation calibration: At each sampling orientation, the resonance peak splitting is calculated using the  $g$ - and hyperfine tensor data from.<sup>15</sup> They are then matched with the magnetic field sweep data collected in the experiment. This procedure results in a very reasonable match between theory and experiment, with only  $\leq 10^\circ$  miss for peak positions as shown in Fig. 3, and thus confirms the validity of the theoretical  $T_m$ -orientation correspondence.

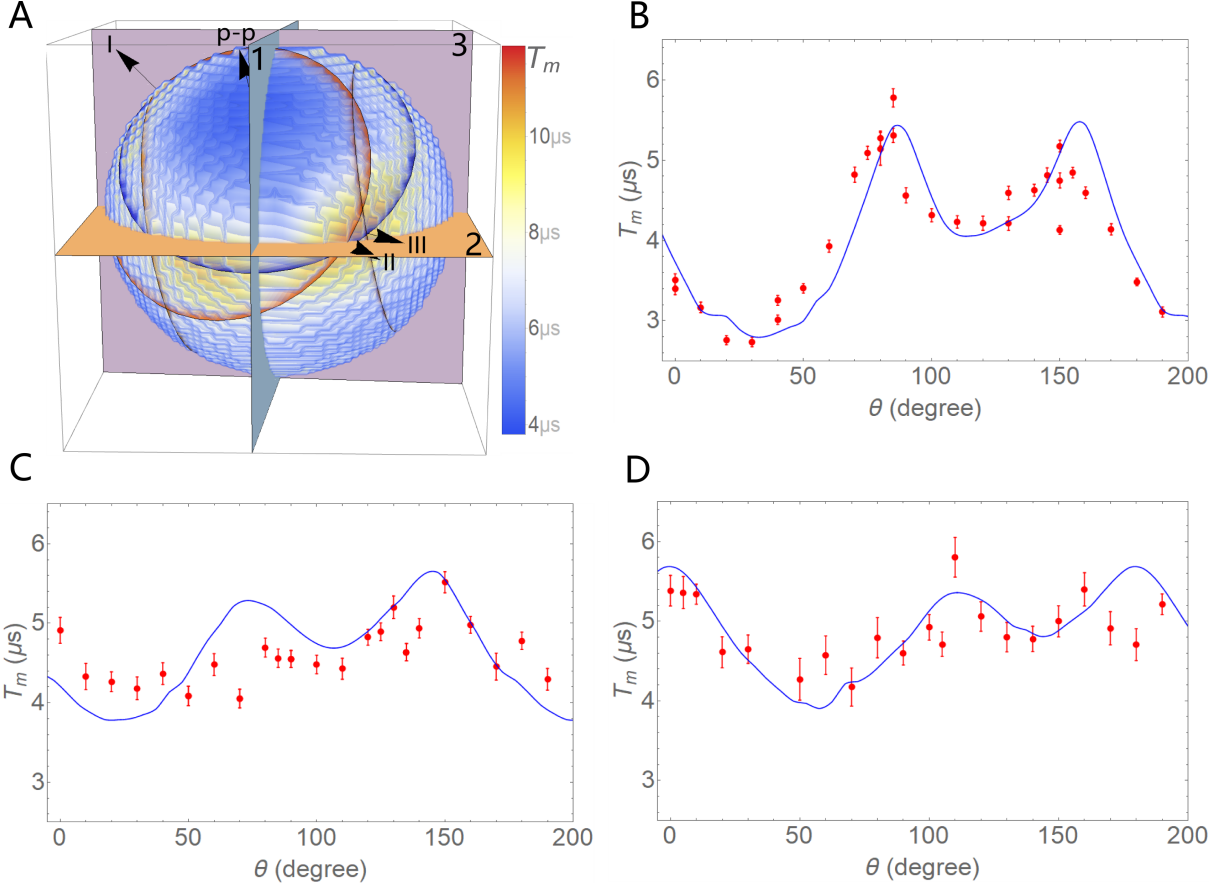


Figure 3: The single crystal pulsed EPR experiment. **A:** Planes 1, 2 and 3 of the MA crystal rotations overlaid on heatmap; **B**, **C** and **D**: the theoretical (blue) and experimental (red) results of the  $T_m$  with respect to the rotation angle  $\theta$  in the crystal rotation planes 1, 2 and 3, respectively.

The second experiment focuses on the removal of the nearest pair alignment by amorphizing MA. As the starting point, nuclear spin bath decay profile for the polycrystalline MA is calculated by averaging over sampling points on a Fibonacci grid, in which each orientation is approximately equally weighted.<sup>14</sup> Approximately 50 points are found to be sufficient

for consistent average. Amorphous phase decoherence decay is estimated using a "plastic crystal" geometry, in which each MA molecule rotates randomly on its lattice position in the  $\beta$ -phase. Theoretical calculation then shows that the electron spin coherence in amorphous MA indeed decays much faster than in polycrystalline.

Experimentally, after extensive tests it is found that  $\beta$ -malonic acid can be amorphorized by mechanical milling with zirconium oxide ( $\text{ZrO}_2$ ) addition. (See supporting information for details.) The Hahn echo decays of electron spins in polycrystalline and amorphous MA are then studied. Both samples are  $\gamma$ -irradiated to create radical concentration of  $4.4 \times 10^{17} \text{ cm}^{-3}$  and  $8 \times 10^{16} \text{ cm}^{-3}$  respectively according to.<sup>16</sup> Electron spin Hahn echo in amorphous sample decays much faster than in polycrystalline MA despite having lower concentration, as shown in Fig. 4. The actual decays are faster than the theoretical estimation, possibly due to the electron-electron spin interactions.<sup>9</sup>

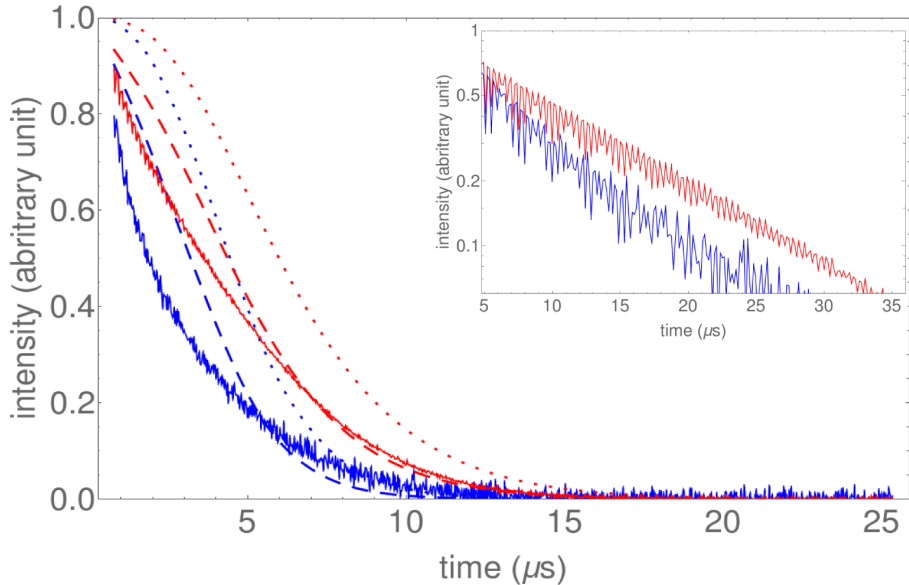


Figure 4: Electron spin Hahn echo decay in polycrystalline (red) and amorphous (blue) MA at 50 K: solid line: experimental signal, normalized by an extrapolated zero time value for comparison with theory; dotted line: nuclear spin bath model calculation result; dashed line: nuclear spin bath result with (partial) corrections for electron-electron spin interaction.<sup>7,10</sup>

As a brief discussion on the major findings of this work, we would like to point out the following: A theoretical survey on the electron spin decoherence decay at various crystal

orientations of single crystal MA is performed using nuclear spin bath model and CCE method. The survey result is confirmed by a standard single crystal pulsed EPR experiment. Our combined theoretical and experimental results prove that the positions of  $T_m$  extrema in single crystal MA coincide with those of the nearest neighbour proton dipolar coupling, first reported in the theoretical computation of P:Si qubit system.<sup>10</sup> Given the difference between P:Si (Fermi contact hyperfine coupling, weak nuclear spin coupling) and MA (dipolar hyperfine, strong nuclear spin coupling) systems, we consider the correspondence universal. Such a simple mechanism then allows a direct connection between structures of the matrix materials and  $T_m$ , making the latter an *in-situ* structure indicator for EPR experiments.

Following the same protocol, the decoherence decay profile of polycrystalline MA is theoretically predicted as average over (survey) orientations. The simple geometrical connection principle then points out further that amorphorization of the same material would reduce  $T_m$  considerably, which is confirmed by the nuclear spin bath model calculation using a plastic crystal geometry. This effect is successfully observed experimentally in a newly produced amorphous MA prepared by mechanical milling.

Positive outcomes of this work convinces us that spin bath model should be considered as the universal framework for electron spin decoherence, in and outside the context of solid state qubits. We also expect that the simple dependence of  $T_m$  to the matrix material structure could be plausible for more future applications.

## Acknowledgement

The authors highly acknowledge the financial support from the Croatian Science Foundation (HRZZ) under the project numbers IP-2013-11-1108, IP-2018-01-3568, IP-2013-11-7423 and IP-2014-09-4744. The Radiation Chemistry and Dosimetry Laboratory (RCDL) at the Ruđer Bošković Institute (RBI) is gratefully acknowledged for providing all  $\gamma$ -irradiated samples. The authors are indebted to Mr. Sc. Željko Marinić from NMR Centre at RBI for measuring

and interpreting the NMR data. We thank Jurica Jurec, Bahar Karadeniz, Dalibor Merunka, Martina Tireli, Srećko Valić, Aleksandar Višnjevac and Dijana Žilić for many supports, discussions and comments during this work.

## Supporting information

### Cut-off scheme

A simple cut-off scheme is used in our CCE calculation: We require the dipolar coupling  $D_{ij}$  to be larger than a threshold value for all  $\{i, j\}$  pairs in each cluster. By this means each cluster order contains all sub-clusters needed for the subsequent orders. A quite large threshold value of  $\sim 1000 \text{ s}^{-1}$  is found to be enough for a stable  $T_m$  prediction in case of Hahn echo. Small threshold values down to  $150 \text{ s}^{-1}$  are tested at single orientations with good consistency, as shown in Fig. 5. The cut-off (in-)dependence suggests that the decoherence decay is more sensitive to short distance clusters than long range ones.

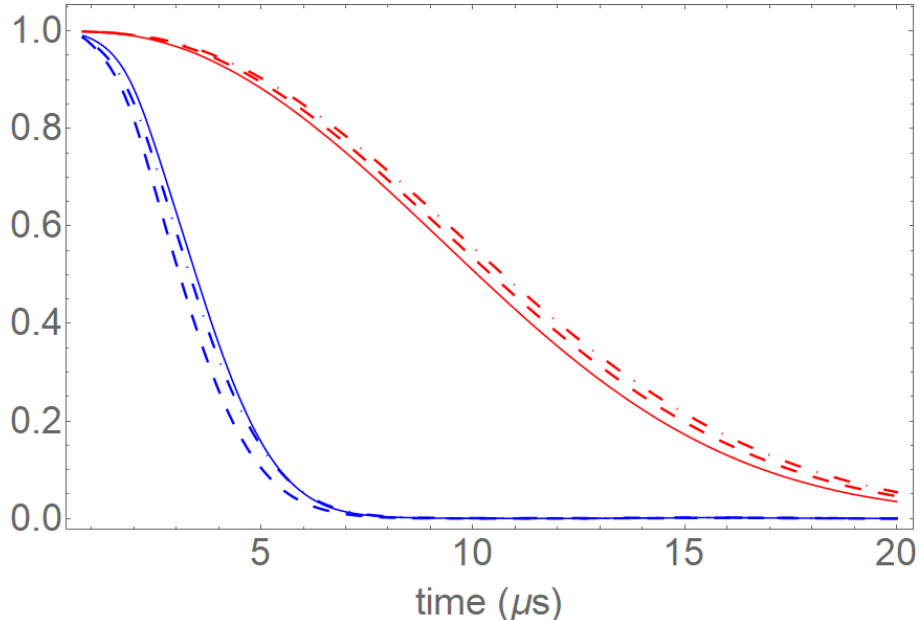


Figure 5: MA radical electron spin Hahn echo decoherence decays in MA proton spin bath, calculated at crystal orientations “I” (red) and “p-p” (blue) in Fig. 2 of the main text using different cut-off values: solid line  $150 \text{ s}^{-1}$ , dashed line:  $1000 \text{ s}^{-1}$ , dot-dashed line:  $1500 \text{ s}^{-1}$ .

## Sample preparation

The MA single crystal was grown by slow evaporation from saturated Milli-Q water solution of polycrystalline MA (Alfa Aesar, 99%) at 277 K. The faces of the crystals were oriented and indexed on a single crystal X-ray diffractometer (Rigaku Oxford diffraction, Xcalibur Nova R) and using CrysAlisPro software.<sup>18</sup> The crystal has four parallel side edges along the b-axis. Of the four side faces, two are found to be parallel to  $b - c^*$  plane. This natural habit of the crystal is used for mounting the crystal in the rotation experiment.

Amorphous MA is prepared by the following method: 250 mg of polycrystalline MA (Alfa Aesar, 99%) and 75 mg of ZrO<sub>2</sub> (Sigma-Aldrich) were placed in 14 mL tungsten carbide milling vessel equipped with one 4.0 g tungsten carbide ball. The milling vessel was cooled in liquid nitrogen and, after cooling for 5 minutes, ground for 90 minutes using laboratory IST-500 (InSolido Technologies) mixer mill operating at 30 Hz. Isolated material was analyzed by powder X-ray diffraction on a PANALYTICAL AERIS X-ray benchtop diffractometer (Bragg-Brentano geometry, 40 kV, 7.5 mA), which confirms that all MA lines are absent in the amorphorized mixture, as shown in Fig. 6.

The nuclear magnetic resonance (NMR) spectra of milled and polycrystalline materials dissolved in dimethyl sulfoxide (DMSO) were also measured, as shown in Fig. 7. Apart from the difference in the respective concentrations, both samples display the same spectral features typical for MA: one peak centred at 12.58 ppm and the other at 3.24 ppm with respect to the tetramethylsilane NMR standard. Other spectral peaks are characteristic of the applied solvent.

All samples (single crystal MA, milled amorphous MA and polycrystalline MA as purchased) were irradiated at the <sup>60</sup>Co source in the Radiation Chemistry and Dosimetry Laboratory (RCDL) at the Ruđer Bošković Institute (Zagreb, Croatia), to a dosage of 1 kGy. All samples were annealed overnight at 340 K in vacuum after irradiation.<sup>17</sup>

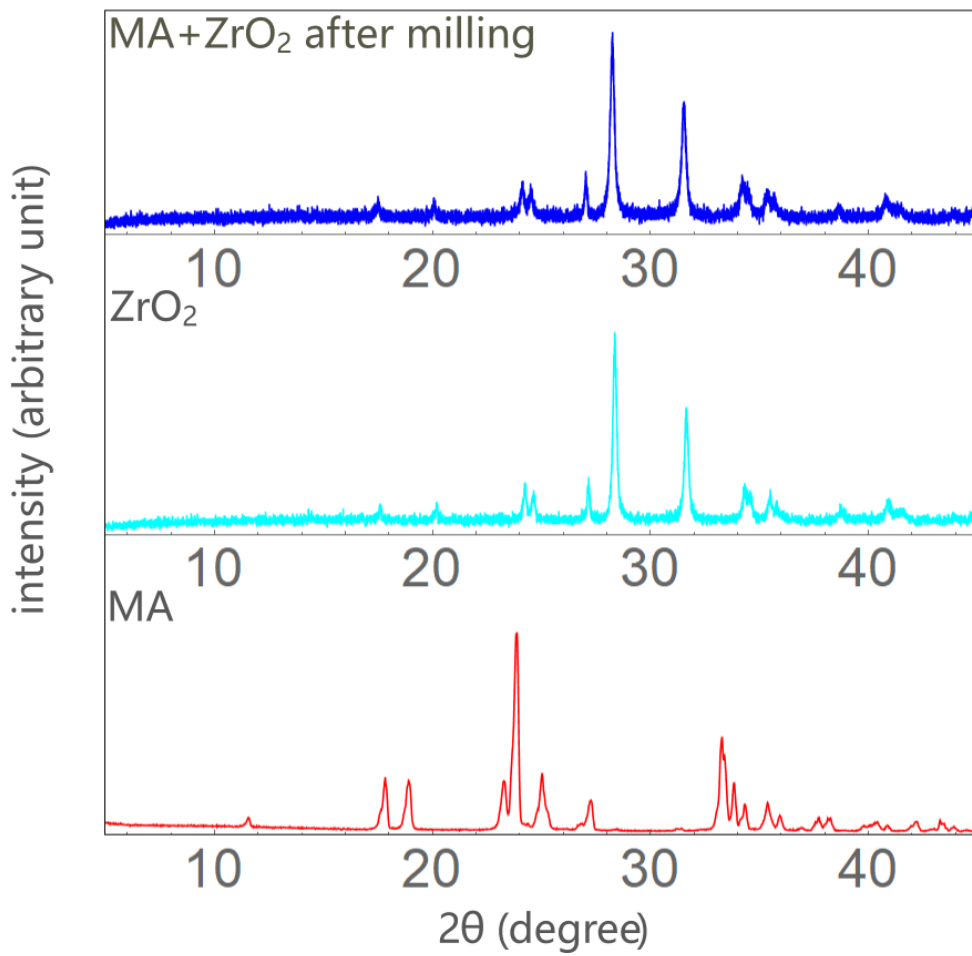


Figure 6: Comparison between the powder X-ray diffraction (XRD) patterns of polycrystalline MA (red), milling additive zirconium oxide (Cyan) and amorphorized MA-zirconium oxide mixture (blue).

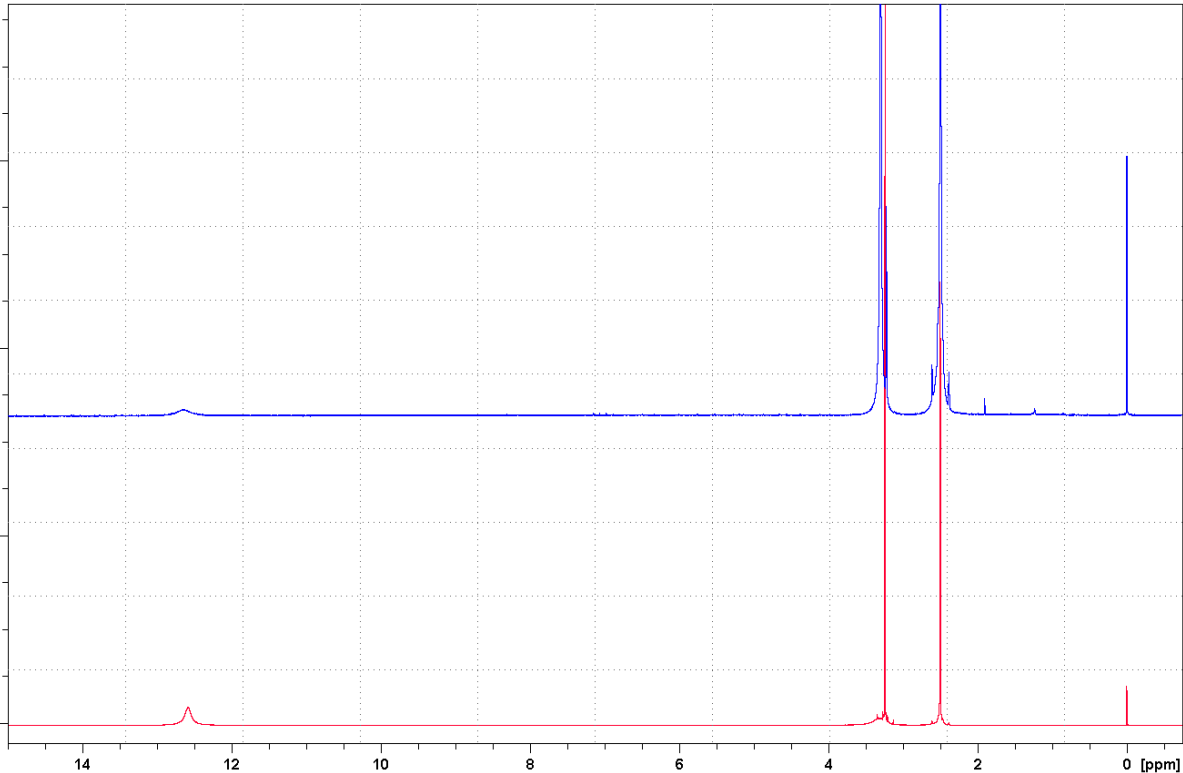


Figure 7: Comparison of NMR spectra of polycrystalline (red) and milled/amorphous (blue) MA acquired using Bruker Avance 600 MHz spectrometer. The samples dissolved in DMSO-d<sub>6</sub> were kept at 298 K, non-spinning. Spectral width was 12019.230 Hz (20 ppm) while 64 scans, 32 K data points per FID and a time delay between pulses of 1 s were applied. Digital resolution was 0.37 Hz. The measured FIDs were Fourier transformed without apodization to the frequency domain spectra.

## EPR measurements

The crystal orientation dependence of  $T_m$  was measured at 80 K on a Bruker ELEXSYS E580 FT/CW X-band EPR spectrometer. According to the crystal habit described above, crystal rotations were set to be around the following three orthogonal axes: 1)  $a' = c^* \times b$ , 2)  $c^* = a \times b$  and 3)  $b$ . An arc of 190° was measured in each rotation. At each orientation EPR spectrum is collected via magnetic field sweep. Time decay of Hahn echo signal was measured at low field peak position using  $\pi$ -pulse duration of 56 ns.  $T_m$ 's were calculated by fitting the recorded data as monoexponential decay.

## References

- (1) Hahn, E. L.; Spin echoes, *Phys. Rev.* **1950**, 80, 580-594, DOI: 10.1103/PhysRev.80.580.  
Carr, H. Y.; Purcell, E. M.; Effects of diffusion on free precession in nuclear magnetic resonance experiments, *Phys. Rev.* **1954**, 94, 630-638, DOI: 10.1103/PhysRev.94.630.  
Meiboom, S.; Gill, D.; Modified spin-echo method for measuring nuclear relaxation times, *Rev. Sci. Instrum.* **1958**, 29, 688-691, DOI: 10.1063/1.1716296.  
Uhrig, G. S.; Keeping a quantum bit alive by optimized  $\pi$ -pulse sequences, *Phys. Rev. Lett.* **2007**, 98, 100504, DOI: 10.1103/PhysRevLett.98.100504.
- (2) Schweiger A.; Jeschke G.; Principles of Pulse Electron Paramagnetic Resonance; Oxford University Press: Oxford, United Kingdom; 2001.
- (3) Yao, W.; Liu, R.-B.; Sham, L. J.; Theory of electron spin decoherence by interacting nuclear spins in a quantum dot, *Phys. Rev. B* **2006**, 74, 195301, DOI: 10.1103/PhysRevB.74.195301.
- (4) For a contemporary review on the state-of-the-art, see Yang, W.; Ma, W. L.; Liu, R.-B.;

Quantum many-body theory for electron spin decoherence in nanoscale nuclear spin baths, *Rep. Prog. Phys.* **2017**, 80, 016001, DOI: 10.1088/0034-4885/80/1/016001.

- (5) Saikin, S. K.; Yao, W.; Sham, L. J.; Single-electron spin decoherence by nuclear spin bath: Linked-cluster expansion approach, *Phys. Rev. B* **2007**, 75, 125314, DOI: 10.1103/PhysRevB.75.125314.
- (6) Yang, W.; Liu, R.-B.; Quantum many-body theory of qubit decoherence in a finite-size spin bath, *Phys. Rev. B* **2008**, 78, 085315, DOI: 10.1103/PhysRevB.78.085315.  
Yang, W.; Liu, R.-B.; Quantum many-body theory of qubit decoherence in a finite-size spin bath. II. Ensemble dynamics, *Phys. Rev. B* **2009**, 79, 115320, DOI: 10.1103/PhysRevB.79.115320.
- (7) du, J. F.; Rong, X.; Zhao, N.; Wang, Y.; Yang, J.; Liu, R. B.; Preserving electron spin coherence in solids by optimal dynamical decoupling, *Nature* **2009**, 461, 1265-1268, DOI: 10.1038/nature08470.
- (8) Zhao, N.; Wang, Z.-Y.; Liu, R.-B.; Anomalous decoherence effect in a quantum bath, *Phys. Rev. Lett.* **2011**, 106, 217205, DOI: 10.1103/PhysRevLett.106.217205.
- (9) Witzel, W. M.; Carroll, M. S.; Cywinski, L.; Das Sarma, S.; Quantum decoherence of the central spin in a sparse system of dipolar coupled spins, *Phys. Rev. B* **2012**, 86, 035452, DOI: 10.1103/PhysRevB.86.035452.  
Witzel, W. M.; Young, K.; Das Sarma, S.; Converting a real quantum spin bath to an effective classical noise acting on a central spin, *Phys. Rev. B* **2014**, 90, 115431, DOI: 10.1103/PhysRevB.90.115431.
- (10) Ma, W.-L.; Wolfowicz, G.; Zhao, N.; Li, S.-S.; Morton, J. J. L.; Liu, R.-B.; Uncovering many-body correlations in nanoscale nuclear spin baths by central spin decoherence, *Nat. Commun.* **2014**, 5, 4822, DOI: 10.1038/ncomms5822.

(11) Zhao, N.; Hu, J.-J.; Ho, S.-W.; Wan, J. T. K.; Liu, R.-B.; Atomic-scale magnetometry of distant nuclear spin clusters via nitrogen-vacancy spin in diamond, *nat. nanotechnol.* **2011**, 6, 242-246, DOI: 10.1038/nano.2011.22.

(12) The structure of  $\beta$ -malonic acid follows Jagannathan, N. R.; Rajan, S. S.; Subramanian, E.; Refinement of the crystal structure of malonic acid,  $\text{C}_3\text{H}_4\text{O}_4$ , *J. Chem. Cryst.* **1994**, 24, 75-78, DOI: 10.1007/BF01665349.

(13) McConnell, H. M.; Heller, C.; Cole, T.; Fessenden, R. W.; Radiation Damage in Organic Crystals. I.  $\text{CH}(\text{COOH})_2$  in Malonic Acid, *J. Am. Chem. Soc.* **1960**, 82, 766-775, DOI: 10.1021/ja01489a002.

(14) González, Á; Measurement of Areas on a Sphere Using Fibonacci and latitude-longitude Lattices, *Math. Geosci.* **2010**, 42, 49-64, DOI 10.1007/s11004-009-9257-x.

(15) Park, D. K.; Feng, G.; Robabeh, R.; Labruyère, S.; Shibata, T.; Nakazawa, S.; Sato, K.; Takui, T.; Laflamme, R.; Baugh, J.; Hyperfine spin qubits in irradiated malonic acid: heat-bath algorithmic cooling, *Quantum Inf. Process* **2015**, 15, 2435-2461, DOI:10.1007/s11128-015-0985-1.

(16) Brustolon, M.; Zoleo, A.; Lund, A.; Spin concentration in a possible ESR dosimeter: an electron spin echo study on X-irradiated ammonium tartrate, *J. Magn. Reson.* **1999**, 137, 389-396, 10.1006/jmre.1998.1671.

(17) Sagstuen, E.; Lund, A.; Itagaki, Y.; Maruani, J.; Weakly Coupled Proton Interactions in the Malonic Acid Radical: Single Crystal ENDOR Analysis and EPR Simulation at Microwave Saturation, *J. phys. Chem. A* **2000**, 104, 6362-6371, DOI: 10.1021/jp000282p.

(18) Rigaku Oxford Diffraction; CrysAlisPro Software system, version 1.171.39.46, **2018**, Rigaku Corporation, Oxford, UK.